Utilizing In-Orbit CYGNSS Roll Maneuvers for Improved Level-1 Calibration—Part I: Application to Direct Signal Channels

Mohammad M. Al-Khaldi, *Member, IEEE*, Scott Gleason, *Senior Member, IEEE*, Christopher S. Ruf, *Life Fellow, IEEE*, Joel T. Johnson, *Fellow, IEEE*, Darren S. McKague, *Member, IEEE*, Anthony Russel, William L. Wells, Tianlin Wang, *Senior Member, IEEE*, Dorina Twigg, Patrick McEnaney, and Joshua Synowiec

***Abstract*—To maintain a healthy power budget, observatories in the Cyclone Global Navigation Satellite System (CYGNSS) constellation routinely undertake commanded roll maneuvers as a means of increasing the exposure of their solar panels to sunlight, thereby boosting power generation levels while continuing normal science operations, in particular Level-1 measurements and related downlinking. The current work (Part I) demonstrates how these roll maneuvers can be leveraged to improve the calibration quality of critical Level-1 observables, achieved primarily through the determination of zenith antenna gain patterns, which receive the direct global positioning system (GPS) signals and GPS transmitter gain tables. In the companion works (Part II and Part III), emphasis is placed on leveraging related techniques to determine the nadir antenna patterns, which receive the reflected GPS signals, and assessing the impacts that updates have on observables. This is enabled by the unique measurement properties that arise due to periodicities in observation geometries when the satellites are rolled compared to their nominal nonrolled state. The proposed technique leads to nonuniform corrections to the CYGNSS zenith antenna patterns by up to 4 dB relative to prior estimates. Uncertainties in the effective isotropic radiated power (EIRP) of the GPS transmissions are reduced by an average of 33%. The calibration improvements highlight the efficacy of leveraging "rolled data" for deriving GPS transmitter patterns, as well as demonstrating that data records as short as a single day can be used with as little as 4% uncertainty in the resulting improvement.**

***Index Terms*—Cyclone Global Navigation Satellite System (CYGNSS), global navigation satellite systems reflectometry (GNSS-R), global positioning system (GPS) effective isotropic radiated power (EIRP), Level-1 calibration, microwave remote sensing.**

Received 9 November 2025; revised 21 February 2026 and 19 April 2026; accepted 27 April 2026. Date of publication 29 April 2026; date of current version 19 May 2026. This work was supported by the National Aeronautics and Space Administration (NASA) Science Mission Directorate through the University of Michigan under Contract NNL13AQ00C. The work of Tianlin Wang was supported by the Jet Propulsion Laboratory, California Institute of Technology through the National Aeronautics and Space Administration under Contract 80NM0018D0004. *(Corresponding author: Mohammad M. Al-Khaldi.)*

Mohammad M. Al-Khaldi and Joel T. Johnson are with the Department of Electrical and Computer Engineering and ElectroScience Laboratory, The Ohio State University, Columbus, OH 43210 USA (e-mail: al-khaldi.2@osu.edu).

Scott Gleason is with Daaxa LLC Consulting Company, Boulder, CO 80307 USA.

Christopher S. Ruf and Darren S. McKague are with the Department of Climate and Space Sciences and Engineering, University of Michigan, Ann Arbor, MI 48109 USA.

Anthony Russel is with Muon Space, Mountain View, CA 94043 USA.

William L. Wells is with the Southwest Research Institute, San Antonio, TX 78238 USA.

Tianlin Wang is with NASA Jet Propulsion Laboratory, California Institute of Technology, Pasadena, CA 91011 USA.

Dorina Twigg, Patrick McEnaney, and Joshua Synowiec are with the Space Physics Research Laboratory, University of Michigan, Ann Arbor, MI 48109 USA.

Digital Object Identifier 10.1109/TGRS.2026.3688948

NOMENCLATURE

α_0	Linearization coefficient.
α_1	Linearization coefficient.
α_2	Linearization coefficient.
b	Bin ratio.
C_Z	Received signal intensity, counts.
$\Delta\theta^Z$	Resolution in θ^Z dimension.
$\Delta\phi^Z$	Resolution in ϕ^Z dimension.
$E^{Z,C}$	EIRP in receiver's direction.
$E^{Z,S}$	EIRP in specular point's direction.
$\tilde{E}^Z$	EIRP anomaly.
Γ_{LR}	Reflectivity.
G^i_{LNA}	LNA gain.
$G^{R,Z,P}$	Assumed receiver antenna gain.
$G^{R,Z*}$	Derived receiver antenna gain.
G_T	Assumed transmitter antenna gain.
G^*_T	Derived transmitter antenna gain.
I_Z.	In-phase component of C_Z.
λ	Electromagnetic wavelength.
Λ	Digital sampling correction function.
μ	Mean.
ν_Z	Scale factor.
P_T	Transmitted signal power.
P_Z	Received signal intensity, watts.
ϕ_Z	Receiver antenna azimuth angle.
φ_r	Receiver roll angle.
Q_Z	In-quadrature component of C_Z.
R_C	Receiver/transmitter range.
ρ^{ref}	Prescribed P_T deviation factor.
σ^0	Normalized bistatic radar cross-section.
σ	Standard deviation.
θ_β	Beta angle.

1558-0644 © 2026 IEEE. All rights reserved, including rights for text and data mining, and training of artificial intelligence and similar technologies. Personal use is permitted, but republication/redistribution requires IEEE permission.
See https://www.ieee.org/publications/rights/index.html for more information.

Authorized licensed use limited to: University of Michigan Library. Downloaded on July 22,2026 at 17:41:03 UTC from IEEE Xplore. Restrictions apply.

θ^B	Transmitter off-boresight angle.
$\theta^{B,Z}$	Angle θ^B toward receiver.
$\theta^{B,S}$	Angle θ^B toward specular point.
θ^Z	Receiver antenna declination angle.
ζ^S	Shape distortion figure of merit.
$[\dots]_r$	Arbitrary variable with roll angle r.

I. Introduction

SPACEBORNE global navigation satellite system reflectometry (GNSS-R) systems are providing new opportunities for meeting the challenges of finer spatial resolution, shorter revisit time, all-weather operation, and mission costs. This is achieved, in part, by using reflections from existing navigation satellites as "illuminators of opportunity" as part of their passive, bistatic, specular operation while concurrently leveraging commercially available components in their construction. Example observatories include the U.K.-Disaster Monitoring Constellation (U.K.-DMC) satellite [1], Technology Demonstration Mission (TDS-1) [2], Cyclone Global Navigation Satellite System (CYGNSS) [3], HydroGNSS [4], the FENGYUN-3 (FY3) series [5] and the Tianmu constellation [6], as well as the Spire Inc. commercial constellation [7] and Muon Space [8] as examples of commercial providers of GNSS-R data.

While the rapid growth of GNSS-R systems in orbit highlights their efficacy, their operation as passive bistatic radars poses calibration challenges. For example, some of CYGNSS's calibration challenges derive from the fact that each of its eight satellites carries port and starboard receive channels capable of tracking four reflections simultaneously, which, in total, amounts to up to 32 DDMs formed over a given integration period. Any channel-specific biases can potentially compromise the consistency of the calibration applied to Level-1 (L1) observations. This is further compounded by the fact that specularly reflected transmissions originate from global positioning system (GPS) space vehicle numbers (SVNs) whose properties are not fully characterized and can change over time.

While prelaunch ground-based characterizations can alleviate some of these uncertainties, the costs associated with fully testing spacecraft flight models (FMs) may be prohibitive and may often inadequately capture in-orbit behaviors, given that the thermal, mechanical, and electromagnetic effects' receivers are impacted by once deployed into low Earth orbit (LEO), all leading to departures from nominal behaviors. This work demonstrates the utility of in-orbit roll maneuvers, over a three-part series, for improving estimates of key Level-1 calibration parameters, including zenith antenna patterns, nadir antenna patterns, and GPS transmitter patterns. The current work (Part I) is concerned with the application of the proposed techniques to receiver zenith channels, which receive direct signal transmissions from the GNSS satellites, while the companion works (Part II and Part III) focus on nadir antenna patterns that receive GNSS signals reflected from the Earth's surface along with the impact this has on observables. While the utility of the proposed techniques generalizes to all GNSS-R receivers, because CYGNSS regularly performs roll maneuvers while concurrently providing the longest continuous GNSS-R data record to date, the constellation's Level-1 measurements are used to demonstrate the approach. Section II discusses why CYGNSS roll maneuvers are necessary. Section III overviews practical considerations and the proposed methodologies. Section IV summarizes the results of the proposed methodologies and discusses the impact that the updated L1 calibration parameters have on key zenith observables. Other considerations are discussed in Section V. A summary of observed trends, lessons learned, and other final conclusions is then provided in Section VI.

While representative examples are selected using observations made by specific CYGNSS receivers originating from a subset of GPS transmitters for the purposes of illustrating the utility of the proposed methodologies, the reported trends generalize across all receivers and transmitters. It is also noted that analysis of the properties of CYGNSS's observations across varied roll maneuvers suggests that they present numerous avenues for the improved calibration of GNSS-R observables. It follows that the methodologies overviewed in this work constitute a limited subset of a wider range of techniques that can be leveraged for the improvement of GNSS-R system calibration quality more generally.

II. Background

CYGNSS FM power demand varies with the spacecraft/sensor mode of operation, typically either nominal science mode (≈25 W) or a Sun-pointing safe mode (≈14 W). Small variations in load occur in response to attitude determination and control system (ADCS) actuator (reaction wheel and torque rod) activity and operational heater cycling. A larger change in instantaneous load of +8 W results from transmitter operation during ground contacts, but this presents only a small increase in orbit-average power (OAP) demand as the ConOps (Concept of Operations) typically calls for one 10-min ground contact per day, per FM.

Power generation capacity, to meet consumption needs, is more variable and is affected primarily by orbit beta angle (θ_β). The parameter θ_β represents the angle between the satellite's orbital plane and a vector to the geocentric position of the Sun. Note that a full listing of the symbols used in this work is available in the Nomenclature. In the safe mode attitude, the largest of three body-fixed solar panels tracks the Sun vector, resulting in steady power generation during the sunlit portion of the orbit. OAP generation is, thus, impacted only by the beta angle due to its effect on eclipse duration. During eclipses, the receivers' solar panels are not directly exposed to sunlight. During nominal science operations, when the FM is flying in its three-axis stabilized, nadir-pointed local vertical, local horizontal (LVLH) relative attitude, the Sun incidence angle on the body-fixed solar panels varies significantly with θ_β. CYGNSS' orbital inclination of 35° combines with Earth's axial tilt to cause θ_β to reach extremes of up to $+/-58.5°$ seasonally, as depicted in Fig. 1.

OAP generation is significantly reduced during high θ_β intervals due to the increased solar angles, despite the eclipse duration being up to 30% shorter at beta extremes compared to when θ_β is zero. Variations in solar irradiance due to Earth's elliptical orbit also impact OAP generation by ±3% annually

Authorized licensed use limited to: University of Michigan Library. Downloaded on July 22,2026 at 17:41:03 UTC from IEEE Xplore. Restrictions apply.

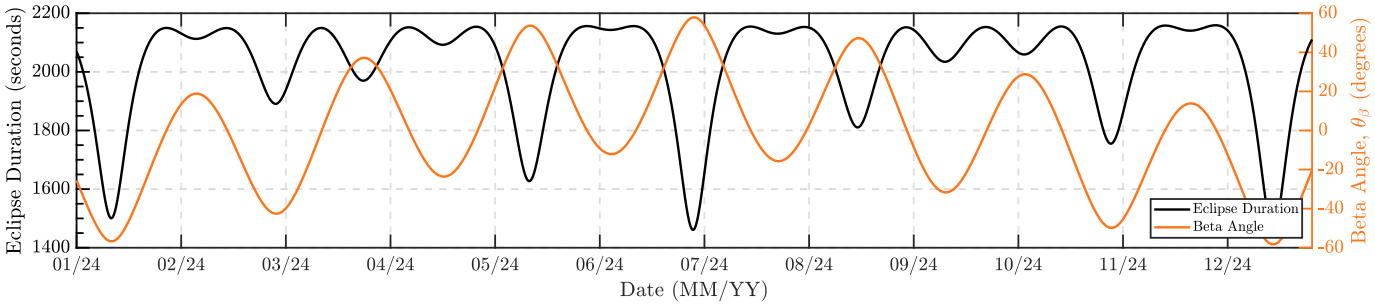


Fig. 1. Time series of typical CYGNSS eclipse duration versus beta angle over the year 2024. Eclipse duration is maximum at $\theta_\beta = 0$ and minimum at θ_β extremes.

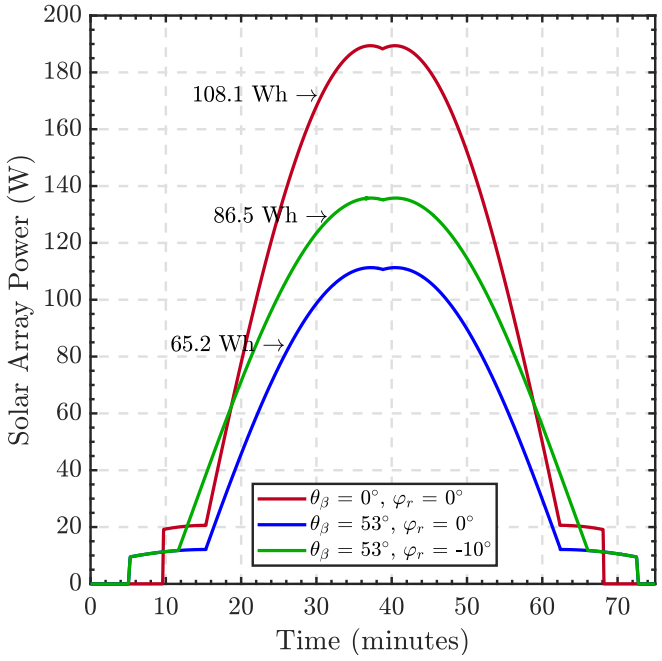


Fig. 2. Solar array power generation levels. A roll offset of $\varphi_r = -10°$ when $\theta_\beta = 53°$ provides a ≈ 33% increase in net power generation for the orbit compared to nominal nadir-pointed science attitude on May 14, 2024. The $\theta_\beta = 0°$ case occurring April 28, 2024, is shown for context.

with the lowest power generation occurring at aphelion in early July.

To ensure that the battery State of Charge (SoC) is maintained at a level sufficient to reliably complete an unexpected transition to Sun-pointing safe mode, a minimum allowable battery SoC (β_{min}) was established prelaunch. β_{min} equates to enough energy in the battery to successfully complete Sun acquisition with three-sigma confidence, assuming no input from the solar array. For low $|\theta_\beta|$ angle periods, the minimum battery SoC, occurring at the end of eclipse during science operations, stays above the established safe SoC level with a positive margin. As $|\theta_\beta|$ increases, that margin is reduced and eventually would become negative, assuming the nominal science attitude. To maintain the minimum safe battery SoC at high beta, the FM is rolled toward the Sun using a fixed roll offset applied in the LVLH frame such that the primary solar panel is tilted toward the Sun, reducing the cosine loss. When $|\theta_\beta|$ is large, a modest roll angle provides a significant boost to OAP generation, as shown in Fig. 2, and recovers the necessary power margins. The very small (18 mNms) reaction wheels employed by CYGNSS afford only a low level of FM agility, such that alternating between nominal nadir-pointing attitude and roll-offset attitudes based on varied levels of Sun versus shadow exposures within every orbit is not attempted. Instead, the roll offset configuration is entered when $|\theta_\beta|$ exceeds a threshold value and is held fixed until $|\theta_\beta|$ drops below the threshold. Fig. 3 shows the effect on battery SoC of using a roll-offset attitude for ≈ 10.5 days centered on a local max of θ_β. The SoC increases from a minimum of ≈ 54% to a maximum of 84% following the roll maneuver.

Rolling when $|\theta_\beta|$ is large to maintain power margin has, therefore, been performed since the beginning of the mission. As the electrical power system (EPS) continues to age, the FMs must spend an ever-increasing fraction of time in the roll-offset configuration. The threshold for when to roll is empirically determined based on the observed minimum battery SoC as a function of θ_β over the prior 6–12 month period. This approach is simple but effective in tracking the unique performance of each CYGNSS FM over time without requiring detailed modeling. An assessment is made for a high θ_β interval near aphelion each year to establish the beta threshold to be used for at least the next 6 months. Within this time, any additional EPS degradation is expected to be countered by the increased solar irradiance heading toward perihelion. Another assessment is typically made each year, late summer or fall, to determine if any changes are warranted prior to reaching aphelion again. An additional 5% of SoC margin is included when establishing the threshold value for θ_β in order to maintain resilience to unexpected pointing excursions that could result in reduced power generation for any given orbit.

As of mid-2025, for each receiver, approximately 100 days of data taken while in a rolled state are available since the CYGNSS launch date.

III. Proposed Approach

The calibration of observables derived from CYGNSS's primary science payload, the delay Doppler mapping receiver (DDMR) [9], relies on the absolute power calibration of all received signal intensities. This includes accounting for GPS SVN-specific effective isotropic radiated power (EIRP) levels [10], [11]. Previous instruments [1], [2], including CYGNSS up to August 2018, have relied on static prelaunch characterizations of SVN properties that include transmit power P_T and gain $G_T(\theta^B)$ at specific off-boresight angles θ^B to provide

Authorized licensed use limited to: University of Michigan Library. Downloaded on July 22,2026 at 17:41:03 UTC from IEEE Xplore. Restrictions apply.

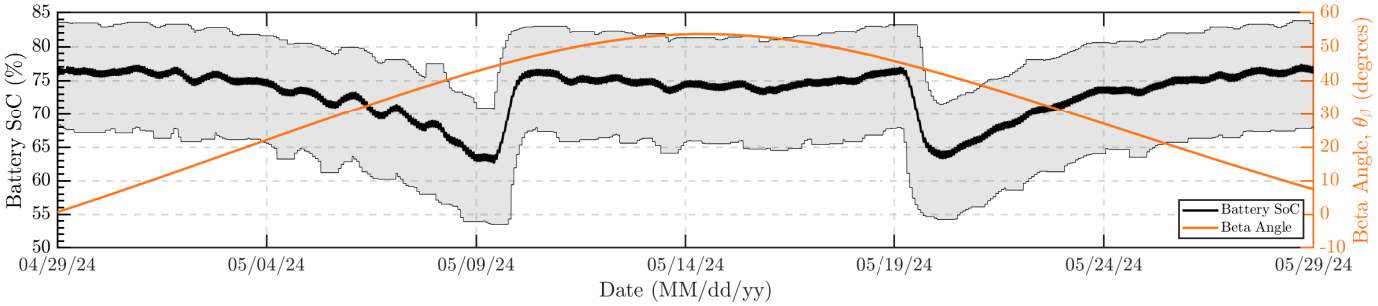


Fig. 3. SoC series highlighting impact of rolling CYGNSS FM3 when $\theta_\beta > 43.5°$ to keep minimum battery state-of-charge above a target value of 53% during a roll maneuver in May 2024. The spacecraft was rolled on May 9 and returned to nadir on May 19. A 10-min moving average window is applied to the SoCs reported every second with the shaded region indicating minimum and maximum values.

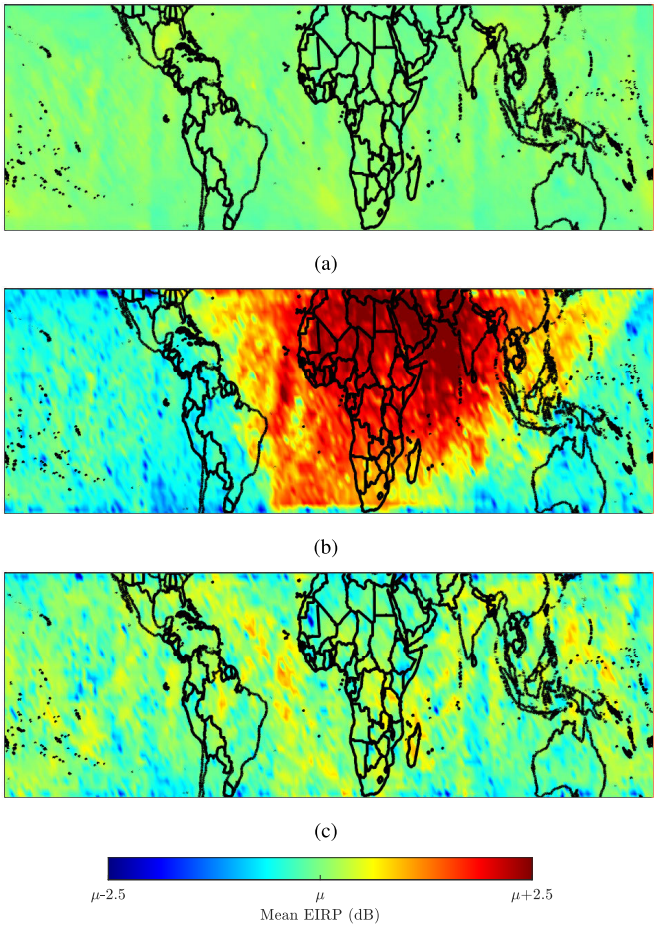


Fig. 4. Mean EIRP for measurements with the angle range $8° \leq \theta^B \leq 10°$ corresponding to block IIF SVNs only. All EIRP maps are reported on a color scale limited to ± 2.5 dB relative to the mean. (a) From static tables, January 2020. Mean EIRP is 30.48 dB. (b) Dynamically tracked, January 2020. Mean EIRP is 32.31 dB. (c) Dynamically tracked, May 2020. Mean EIRP is 31.59 dB.

the necessary inputs as part of relevant L1 calibration and validation activities. These inputs have been shown to be inadequate [12], [13], particularly over regions containing terrestrial GPS interference sources [15], as transmit power from specific SVNs can be routinely varied as a countermeasure. An example of this is shown in Fig. 4 where static estimates are shown to differ from "true" EIRP levels in plot (b) by up to 5 dB. In turn, the reliance on these characterizations of transmitter properties would have introduced commensurate

TABLE I
CHANNEL-SPECIFIC INSTRUMENT ν_Z SCALING FACTORS

FM→	1	2	3	4	5	6	7	8
	-1.62	-1.60	-1.56	-1.63	-1.30	-1.98	-1.63	-1.66

calibration errors to CYGNSS observables, namely, the normalized bistatic radar cross-section σ^0 and left-hand circularly polarized reflectivity Γ_{LR}. While the analysis of recent trends suggests that the majority of GPS transmitters have ceased operating in a "flex power" mode as of March 2020, as shown in Fig. 4(c), the desire to accurately calibrate the mission's complete data motivate exploring the means with which channel calibration parameters may be improved. This is informed by considerations relating to times when SVN-specific P_T levels were not constant as well as the potential for related commanded power shifts to resume "flex power" operation.

To facilitate tracking EIRP in real time, lower-gain patch antennas mounted on each of CYGNSS's receivers, originally intended to provide navigation solutions, were repurposed to serve as power monitors [12], [13]. This poses the challenge of calibrating the zenith channels' in-phase (I_Z) and in-quadrature (Q_Z) signal intensities measured in units of raw counts to a received signal power P_Z in watts or equivalently dBw. To achieve this, a raw count signal intensity in decibels is initially computed using

$$C_{Z,dB} = \frac{10 \log_{10}\left(\sqrt{I_Z^2 + Q_Z^2}\right)}{1 - \nu_Z\,(1 - \Lambda\,(b))}. \quad (1)$$

As automatic gain control is deactivated to achieve these zenith absolute power measurements, discretization artifacts associated with CYGNSS's 2-bit analog-to-digital converters (ADCs), depending on input signal intensities, have been shown to occur [16]. The factor $(1 - \nu_Z(1 - \Lambda(b)))$ in (1) compensates for these effects depending on each measurement's quantized intensity distribution in the four digital states ± 1 and ± 3 captured through the quantity b. The factor b is the ratio of the number of samples in ± 1 states compared to those in the ± 3 states over the integration period, and the function Λ is

$$\Lambda\,(b) = -0.0025\,b^3 + 0.0359\,b^2 - 0.3473\,b + 1.61. \quad (2)$$

Authorized licensed use limited to: University of Michigan Library. Downloaded on July 22,2026 at 17:41:03 UTC from IEEE Xplore. Restrictions apply.

The channel-specific ν_Z scale factors listed in Table I are intended to account for each of the eight zenith channels' respective front-end gains and related uncertainties. For a comprehensive overview, see [16]. A spare bench top receiver (a replica of in-orbit hardware) was also used to determine coefficients a_0, a_1, and a_2 required to "linearize" the relationship of measured counts to power in decibels above 1-W $P_{Z,dB}$

$$P_{Z,dB} = a_0 \cdot C_{Z,dB}^2 + a_1 \cdot C_{Z,dB} + a_2. \tag{3}$$

Values of $a_0 = 0.012$, $a_1 = -0.51$, and $a_2 = -1.51$ were found appropriate in these tests. CYGNSS's measured EIRP $E^{Z,C}$ is then given by the following equation:

$$\begin{aligned} E^{Z,C} &= P_T G_T\left(\theta^{B,Z}\right) \\ &= \frac{(4\pi R_C)^2}{\lambda^2} \frac{10^{P_{Z,dB}/10}}{G_{LNA}^i G^{R,Z,p}\left(\theta^Z, \phi^Z\right)} \end{aligned} \tag{4}$$

where R_C is the line of sight range between the CYGNSS receiver and GPS transmitter, λ is the 0.19 m wavelength at the 1.575-GHz L1 frequency of operation, G_{LNA}^i is the zenith channel low-noise amplifier (LNA) gain, and $G^{R,Z}(\theta^Z, \phi^Z)$ is the zenith antenna gain at declination angle θ^Z and azimuth angle ϕ^Z. While the resulting $E^{Z,C}$ estimate is an effective measure of an SVN's EIRP (i.e., the product of its transmit power P_T and transmitter gain G_T at the off-boresight angle pointing in the receiver's direction $\theta^{B,Z}$), it is the EIRP in the direction of the specular point that is of interest for the calibration of σ_0 and Γ_{LR}. Because EIRP levels at the specular point $E^{Z,S}$ are not measured directly, equivalent estimates can be derived through a remapping procedure that accounts for the different transmitter gain levels at the two different angles

$$E^{Z,S} = E^{Z,C} \frac{G_T\left(\theta^{B,S}\right)}{G_T\left(\theta^{B,Z}\right)} \tag{5}$$

where $\theta^{B,S}$ is the off-boresight angle toward the specular point. For completeness, it is emphasized that $\theta^{B,Z}$ is a measure of the angular separation between a vector pointing from the transmitter to the center of the Earth and a vector pointing from the transmitter to a CYGNSS receiver. Conversely, $\theta^{B,S}$ is a measure of the angular separation between a vector pointing from the transmitter to the center of the Earth and a vector pointing from the transmitter to the specular point.

Because the need to use CYGNSS's zenith channels for tracking GPS EIRPs only became evident after launch, patterns corresponding to each receiver's patch antennas were not characterized, and only a best guess derived from chamber measurements using an FM's mock-up, refined through a variety of techniques [17], was available for use as part of the corresponding calibration procedures. Closely related is the fact that while chamber measurements can provide reliable estimates of the zenith antenna patterns in a controlled environment, the process of stowing the satellites prelaunch, the mechanical vibrations the various components undergo as part of the launch and deployment procedures, as well as the ±300 °C temperature variations the exterior of the receivers regularly experience, all creates departures of in-orbit behaviors compared to prelaunch characterizations. In addition, while a number of GPS EIRP patterns parameterized as a function of off-boresight angles have been made publicly available, many are impacted by similar sources of uncertainty. It is, therefore, of interest to develop methodologies that enable deriving more realistic in-orbit behaviors.

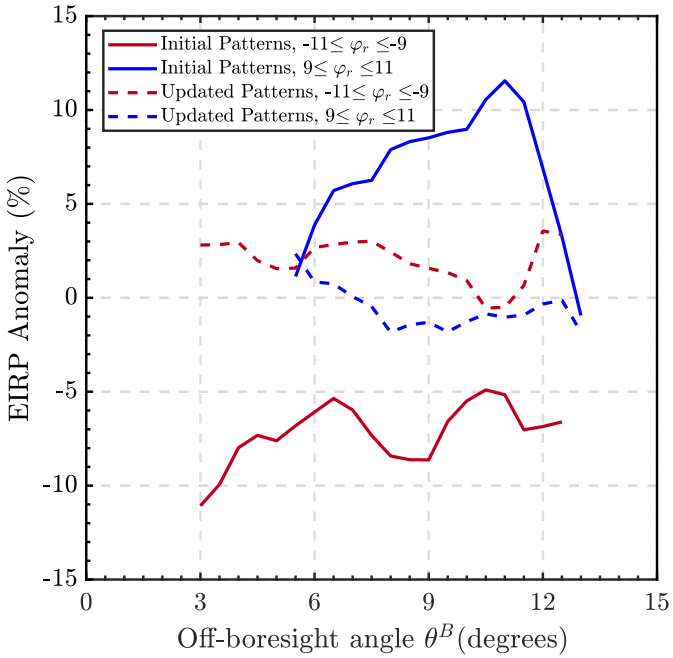


Fig. 5. FM01 and EIRP anomalies for tracked reflections originating from SVN41 transmissions at roll angles $\varphi_r = +10°$ and $\varphi_r = -10°$. View is limited to the range of off-boresight angles over which 90% of the measurements exist. Initial patterns refer to estimates of the zenith antenna gains that are not informed by any rolled data.

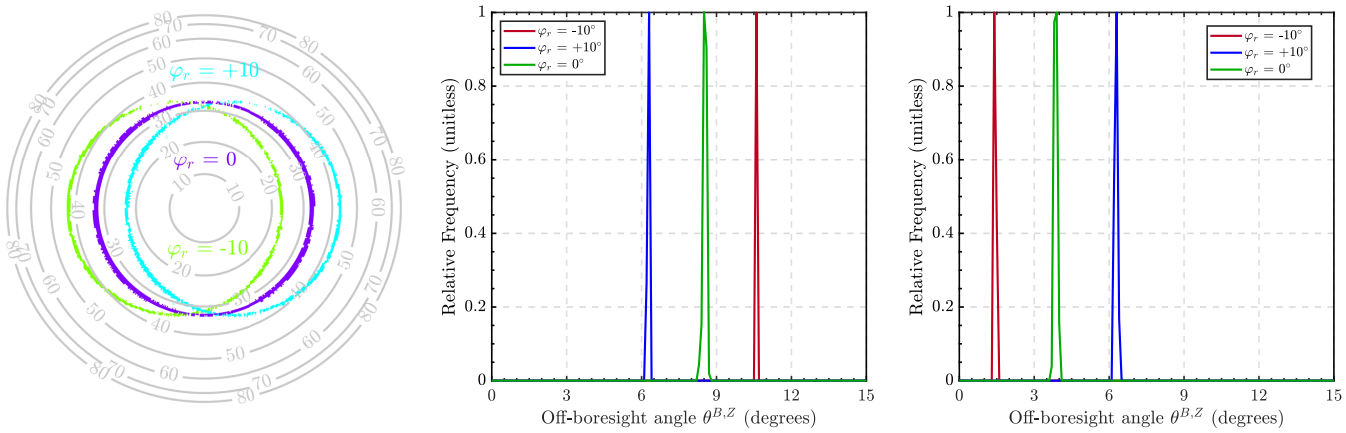
To highlight these uncertainties, consider the EIRP trends summarized in Fig. 5. Using the mean $E_r^{Z,S}$ taken at roll angles $-9° \le \varphi_r \le -11°$ (i.e., $\varphi_r = -10°$) and $9° \le \varphi_r \le 11°$ (i.e., $\varphi_r = +10°$), differences were computed relative to the mean $E_0^{Z,S}$ at $\varphi_r = 0°$ and expressed as a function of the off-boresight angle $\theta^{B,S}$ using observations specific to FM01 and SVN41

$$\tilde{E}^{Z,S}\left(\theta^{B,S}\right) = \frac{\frac{100}{N_r}\sum_{i=1}^{N_r} E_r^{Z,S}\left(\theta^{B,S}\right) - \frac{100}{N_0}\sum_{i=1}^{N_0} E_0^{Z,S}\left(\theta^{B,S}\right)}{\frac{1}{N_0}\sum_{i=1}^{N_0} E_0^{Z,S}\left(\theta^{B,S}\right)} \tag{6}$$

where N_0 and N_r are the number of samples available at a given off-boresight angle in the nonrolled and rolled states, respectively. The "EIRP anomaly" is then given by $\tilde{E}^{Z,S}$.

While it is reasonable to expect the EIRP to vary by extents commensurate with the change in transmitter gain across the various $\theta^{B,Z}$ angles, at a fixed off-boresight angle, the anomalies observed, ranging between ±10% are indicative of the impacts of calibration uncertainty. At $\theta^{B,Z} = 8°$, as an example, the EIRP pattern locations observed in the three different roll states are depicted in Fig. 6(a). The specific receiver–transmitter observation geometries included cause the measurements to map to unique, generally nonintersecting, segments of the zenith antenna pattern. As a result, consistent mean underestimation and overestimation of $G^{R,Z}(\theta^Z, \phi^Z)$ at the respective polar regions spanned at the roll states + 10 and −10 relative to those at zero roll give rise to the anomalies noted in Fig. 5.

Authorized licensed use limited to: University of Michigan Library. Downloaded on July 22,2026 at 17:41:03 UTC from IEEE Xplore. Restrictions apply.



(a) (b) (c)

Fig. 6. Illustration of geometry periodicities and reciprocal properties across different roll angles generated using a data record extending from January 2019 to August 2025. (a) Locations in polar coordinates of FM01-SVN70 measurements whose off-boresight angles fall in the range $7.9° \leq \theta^{B,Z} \leq 8.1°$ for measurements collected with FM01 roll angles of $\varphi_r = 0$, +10, and −10. (b) Densities of measurements falling across a range of off-boresight angles as a function of roll angles for zenith measurements made at $\theta^Z = 35°$ and $\phi^Z = 90°$. (c) Densities of measurements falling across a range of off-boresight angles as a function of roll angles for zenith measurements made at $\theta^Z = 15°$ and $\phi^Z = 260°$.

At a fixed location in the zenith antenna pattern, the same basic relationships allow the gain at a single polar angle to be associated with observations made at three distinct off-boresight angles across the three roll states. Examples of this are shown in Fig. 6(b) and (c) for directions $\theta^Z = 35°$, $\phi^Z = 90°$ and $\theta^Z = 15°$, $\phi^Z = 260°$. The two uniquely map to observations made at off-boresight angles 6.5, 8.5, 10.5 and 1.5, 3.5, 6.5, respectively. For each zenith direction, defined in this work as having resolutions $\Delta\theta^Z = 0.1°$ and $\Delta\phi^Z = 0.2°$, these basic observation geometry-related dependencies are leveraged for deriving improved zenith antenna patterns and GPS G_T estimates.

Observations made in a single roll state traverse the zenith polar space at arbitrary locations that map to all off-boresight angles only when both $G^{R,Z}$ and G_T vary. The sampling of a transmitter's G_T curve, however, occurs at multiple "locations" (i.e., $\theta^{B,Z}$), given the dependencies of in Fig. 6, for which the zenith antenna direction remains fixed, allowing EIRP variability to be more unambiguously mapped to G_T changes.

It is assumed that over periods where SVNs were not operated in a "flex power" mode, each transmitter's P_T is a constant. For a receiver's zenith pattern in direction θ^Z, ϕ^Z, there then exist antenna gain levels $G_r^{R,Z}$ and $G_T(\theta_r^B)$ whose product lies along contours that satisfy the inequalities

$$\left| \frac{E_0^{Z,C} G^{R,Z,p}\left(\theta^Z, \phi^Z\right)}{G_T\left(\theta_0^B\right) G_0^{R,Z}\left(\theta^Z, \phi^Z\right)} - P_T \right| \leq \rho^{ref} P_T \tag{7}$$

$$\left| \frac{E_{+10}^{Z,C} G^{R,Z,p}\left(\theta^Z, \phi^Z\right)}{G_T\left(\theta_{+10}^B\right) G_{+10}^{R,Z}\left(\theta^Z, \phi^Z\right)} - P_T \right| \leq \rho^{ref} P_T \tag{8}$$

$$\left| \frac{E_{-10}^{Z,C} G^{R,Z,p}\left(\theta^Z, \phi^Z\right)}{G_T\left(\theta_{-10}^B\right) G_{-10}^{R,Z}\left(\theta^Z, \phi^Z\right)} - P_T \right| \leq \rho^{ref} P_T \tag{9}$$

where the subscript r denotes roll state, P_T is an SVN-specific transmit power level from a ground-based power monitor [12], and $G^{R,Z,p}$ is an existing estimate of gain levels; this can be any assumed representation of the in-orbit patterns used as part of the calibration procedure. In the case of CYGNSS, existing estimates are based on chamber measurements of the zenith patch antenna mounted on a mock-up of a spare CYGNSS FM. These are then supplemented with additional ancillary information relating to the properties of SVNs whose reflections are tracked. For a more comprehensive overview, see [12] and [13]. Initial characterizations are thought to be coarse as they do not include deployed solar panels or internal electronics. These initial gain estimates are not informed by data taken, while the receivers are rolled. The $E_r^{Z,C}$ estimates in (7)–(9) are means of available estimates, given a particular transmitter/receiver pair, roll state, and polar coordinate. The product of the EIRP term with the $G^{R,Z,p}$ term, therefore, indicates that no gain correction is initially applied as part of the calibration process. Expressions (7)–(9) explore what combination of zenith antenna gain values (at a fixed zenith polar coordinate) and transmit gain levels at the relevant off-boresight angles allows for a measured transmit power solution that is consistent within a margin ρ^{ref} with known values of P_T across all three roll states. Overly restrictive margins ρ^{ref} have been found to limit the capacity to derive antenna gain solutions across the full polar spaces of the eight zenith channels, while overly permissive thresholds do not adequately address the desire to ensure EIRP consistency. Associated tests suggested that $\rho^{ref} = 10\%$ is adequate.

The terms $G_0^{R,Z}$, $G_{+10}^{R,Z}$, and $G_{-10}^{R,Z}$ are the roll angle-specific sets of potential zenith gain solutions at θ^Z, ϕ^Z, which, in part, facilitates meeting the ρ^{ref} threshold. The resulting departures from the assumed P_T as a function of receiver and transmitter gains are reported in Fig. 7(a) and (b) where, for every roll state, the combination of properties that satisfy the 10% error requirement is indicated by the color-coded contours. It is observed that they span distinct spaces. For example, at a transmit gain value of 12.5 dB, valid $G_0^{R,Z}$ solutions extend from 1.07 to 1.92 dB, while those at $G_{+10}^{R,Z}$ and $G_{-10}^{R,Z}$

Authorized licensed use limited to: University of Michigan Library. Downloaded on July 22,2026 at 17:41:03 UTC from IEEE Xplore. Restrictions apply.

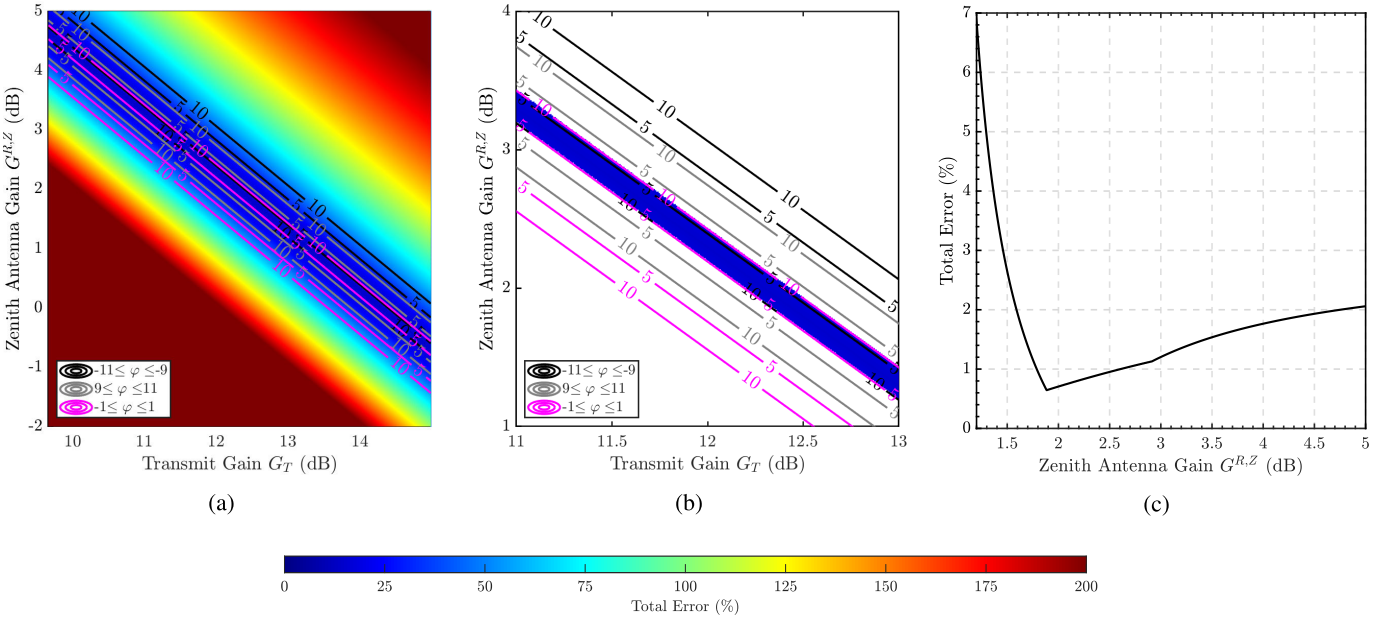


Fig. 7. Illustration of constraints the availability of rolled data places on potential zenith antenna gain solutions. Color coded contours indicate the limits, which ensure that $\rho^{ref} = 10\%$ relative to an assumed P_T level for SVN 41 using FM01 observations at $\theta^Z = 4°$ and $\phi^Z = 13°$ across the three roll collection states. (a) Complete solution space. (b) View is limited to the subset of FM01 antenna gain solutions that concurrently satisfy error requirements across all roll angles. (c) Cost function used to derive final antenna gain levels for this example polar pixel.

extend from 1.35 to 2.27 and 1.65 to 2.65 dB, respectively. It is instructive to reiterate that the mapping at fixed zenith antenna polar coordinates θ^Z, ϕ^Z occurs relative to the three distinct off-boresight angles θ^B_0, θ^B_{+10}, and θ^B_{-10} at the three roll states and, in turn, three distinct transmitter gain levels such that it is to be expected that the contours span slightly different solution spaces. However, true in orbit $G^{R,Z}(\theta^Z, \phi^Z)$ are a property of the receiver's antenna and are independent of the transmitter's gain levels such that a gain estimate is subsequently selected based on the value that minimizes error relative to the assumed P_T across all three roll states on average

$$*arg\,min_{G^{R,Z*}} \frac{1}{P_T N_{G_T}} \sum_{i=1}^{N_{G_T}} \sum_{r=1}^{3} \left| \frac{E_r^{Z,C}(i)\, G^{R,Z,p}}{G_T\left(\theta_r^B; i\right) G^{R,Z}\left(\theta^Z, \phi^Z\right)} - P_T \right| \tag{10}$$

where N_{G_T} corresponds to the number of possible transmitter gain solutions $G_T^*(\theta_r^B)$ that are limited to the range $G_{T,ref}(\theta_0^B) - 0.5\ G_{T,ref}(\theta_0^B) \le G_T^*(\theta_r^B) \le G_{T,ref} + 0.5\ G_{T,ref}(\theta_0^B)$ utilizing published ancillary information relating to reference GPS antenna patterns whose gains are $G_{T,ref}$ to initially constrain solutions. An example output from this process is shown in Fig. 7(c) where a clear minima at 1.88 dB occurs and is assigned the $G^{R,Z}(\theta^Z, \phi^Z)$ value. Importantly, the procedure is conducted for each receiver, zenith pixel, and SVN separately. As a result, for each CYGNSS zenith channel, more than 30 patterns corresponding to the number of SVNs whose reflections were tracked are produced; the final zenith antenna pattern is the average of all available patterns. Once a receiver gain solution $G^{R,Z}$ at angles θ^Z, ϕ^Z for a given zenith channel is obtained, initial solutions G_{Ti}^* for each SVN's gain curve at the angles mapping in roll are then developed using

$$G_T^*\left(\theta_0^B\right) = \frac{E_0^{Z,C} G^{R,Z,p}}{P_T G^{R,Z}\left(\theta^Z, \phi^Z\right)} \tag{11}$$

$$G_T^*\left(\theta_{+10}^B\right) = \frac{E_{+10}^{Z,C} G^{R,Z,p}}{P_T G^{R,Z}\left(\theta^Z, \phi^Z\right)} \tag{12}$$

$$G_T^*\left(\theta_{-10}^B\right) = \frac{E_{-10}^{Z,C} G^{R,Z,p}}{P_T G^{R,Z}\left(\theta^Z, \phi^Z\right)}. \tag{13}$$

At the same off-boresight angle, using the same antenna, thousands of independent G_T^* estimates are developed as the "rings" in Fig. 6(a), indicating that the relevant zenith antenna pixels are traversed. The volume of estimates is further expanded when accounting for inputs from all eight observatories as the properties of a given SVN gain curve are independent of those of the CYGNSS observatories such that the final gain levels at a given off-boresight angle are the average of all available estimates.

To summarize, the procedure broadly entails the steps.

1) Identify the unique off-boresight angles that the availability of the rolled data provides. In this work, data from the three $\varphi_r = 0, +10, -10$ main roll states are used.
2) Compute mean measured EIRP across the available roll states (or, equivalently, roll angles).
3) Invert measured EIRP to measured P_T by rearranging the terms in (4).
4) Identify the appropriate zenith antenna gain value that will minimize the difference between measured P_T and a reference P_T across all available off-boresight angles or equivalently roll states using (10).

Authorized licensed use limited to: University of Michigan Library. Downloaded on July 22,2026 at 17:41:03 UTC from IEEE Xplore. Restrictions apply.

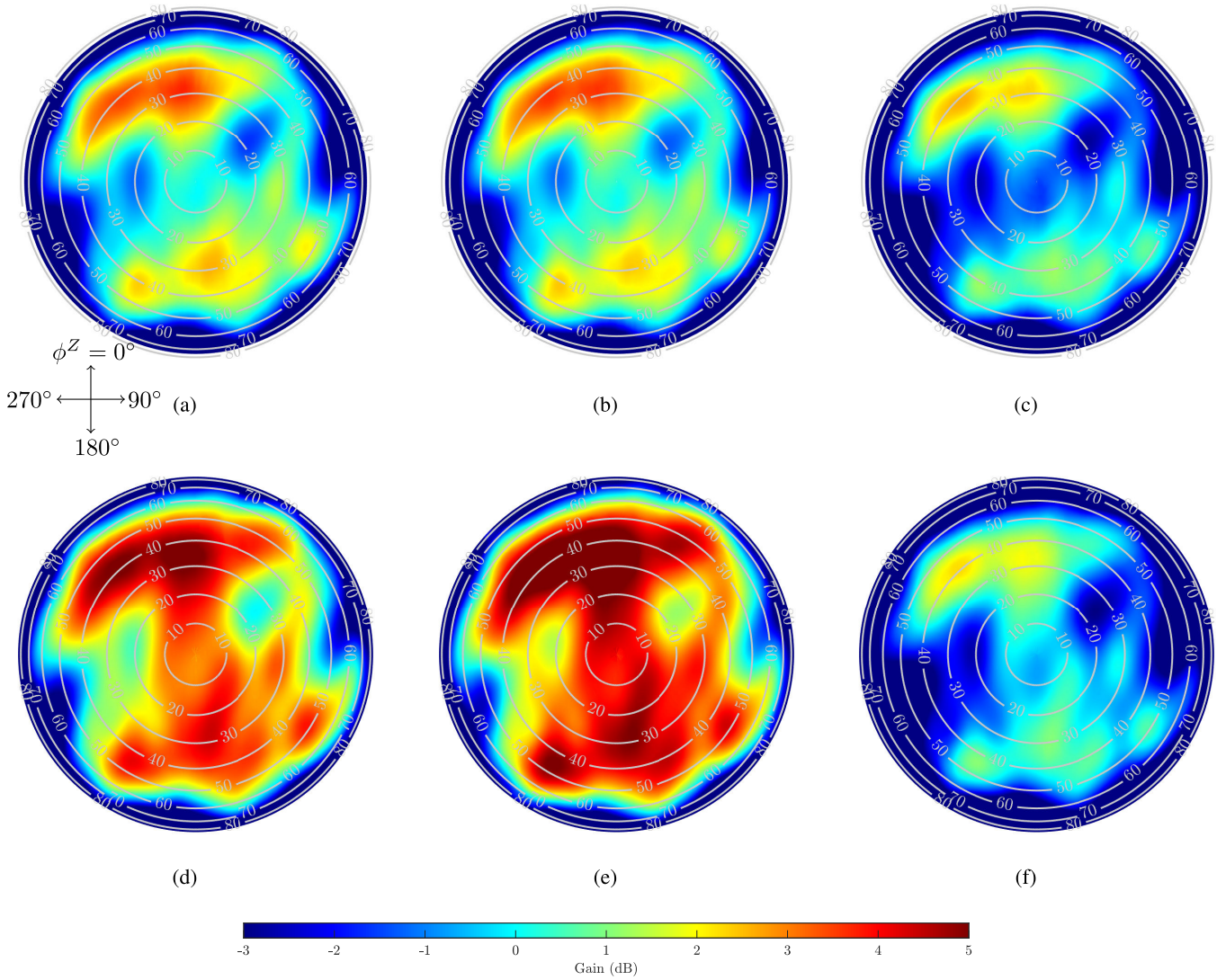


Fig. 8. Comparisons of example zenith gain patterns. Satellite flight direction is along $\varphi = 0°$. (a) Initial, FM01. (b) Initial, FM02. (c) Initial, FM05. (d) Updated, FM01. (e) Updated, FM02. (f) Updated, FM05.

5) Using the zenith antenna gain solution, estimate the transmitter antenna gains at the relevant off-boresight angles using (11)–(13).

These steps are pursued separately for every polar pixel and for every unique receiver/transmitter pairing. To avoid the ambiguities that "flex power" events may introduce, CYGNSS observations acquired after February 2020 are used in the development of all solutions.

IV. Observed Trends

A. Zenith Antenna Patterns

Examples of the derived zenith antenna patterns compared to the initial estimates for receivers FM01, FM02, and FM05 are depicted in Fig. 8. An initial examination highlights a number of similarities between the two sets of patterns. For example, in both sets, the higher gain levels occur in the azimuth space $-50 \leq \phi^Z \leq 10°$ and $20 \leq \theta^Z \leq 50$, while a secondary set of maxima occurs in the polar space circumscribed by $170 \leq \phi^Z \leq 210°$ and $20 \leq \theta^Z \leq 50$. It is helpful to recall that the zenith antennas are square patches sandwiched between two starboard- and port-oriented solar panels. As a result, coupling and multipath effects in the near-field are thought to distort the antenna patterns such that gain levels are reduced in both directions, while the spaces parallel to the receivers' velocity vectors maintain higher gain levels. Noteworthy distinctions, however, include the fact that peak gains in the case of FM01 are thought to be on the order of 5.2 dB, using the methodologies overviewed in Section III, while existing initial estimates suggest that the peak was closer to 3.7 dB. Across the eight zenith channels, it is FM02 that is found to have the highest overall gain levels approaching 6.02 dB as evidenced by the elevated gains spanning the complete polar space in Fig. 8(e) compared to its counterpart in (b). Less variation is observed in the overall gain levels of FM05 where initial estimates suggest peak gains are on the order of 2.6 dB with the updated patterns suggesting 2.2 dB. While the trends summarized in Fig. 8 are instructive, the

Authorized licensed use limited to: University of Michigan Library. Downloaded on July 22,2026 at 17:41:03 UTC from IEEE Xplore. Restrictions apply.

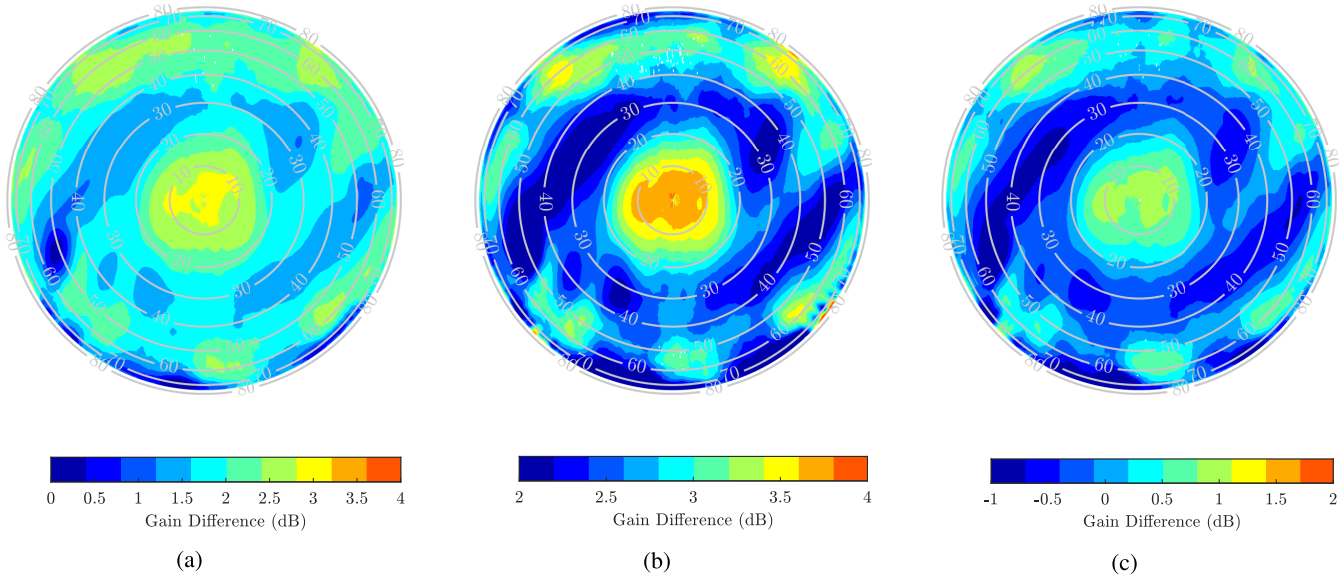


Fig. 9. CYGNSS zenith antenna gain difference levels computed as $G_{updated} - G_{existing}$. (a) FM01. (b) FM02. (c) FM05.

differences in gain pattern structures are more complex than shifts in mean gain levels. This is illustrated in Fig. 9 across the same three FMs. While it is important to achieve accurate power calibration by compensating for zenith gains at the appropriate levels, shifts in the overall gain by a constant factor do not significantly compromise calibration quality and instead simply introduce an FM-specific bias. Conversely, it is the nonuniform shifts, the majority of which vary from 1.20 to 2.83, 2.00 to 3.68, and −0.70 to 0.87 dB for FM01, FM02, and FM05, respectively, which increase the standard deviation of measured EIRPs and introduce shape distortions, examples of which were alluded to in Fig. 5 and more significantly impact calibration quality.

Closely related are uncertainty statistics associated with the updated patterns. For each of the eight final solutions, 35 patterns corresponding to the SVNs whose measurements were initially incorporated were generated. The associated variability reported as the ratio of the standard deviation relative to the mean (σ/μ) of the three example patterns is reported in Fig. 10, which is projected onto the same polar frame. To provide context for the observed distributions, relative measurement densities are also reported in Fig. 10. No significant FM-to-FM variability in terms of solution uncertainties is noted with the majority of estimates having their variability limited to ≈ 0.15, highlighting the repeatability of gain levels derived from the procedure described in Section III. However, more significant uncertainties are noted over the polar spaces circumscribed by $-30^\circ \leq \phi^Z \leq 30^\circ$ and $165^\circ \leq \phi^Z \leq 195^\circ$. An examination of the measurement density plots depicted in Fig. 10(d)–(f) makes clear that this is associated with a dearth of measurements in those regions where less than 5% of the overall volume of data exists. The concentration of measurements about the azimuths 90° and 270° is more directly related to the operation of the DDMR's specular point tracker, prioritizing measurements in the starboard and port directions where higher nadir antenna gain levels exist, and the likelihood of forming a specular geometry with a GPS transmitter is considerably higher. As a byproduct of this process, the regions of the zenith pattern with the higher gain levels are utilized less frequently in real-time EIRP tracking. For this reason, in the process of deriving the final zenith antenna patterns, a minimum number of measurements per polar pixel requirement of 500 observations is enforced. For pixels where this requirement cannot be met, the corresponding gain levels are determined through nearest neighbor interpolation and, where necessary, extrapolation.

B. GPS Transmit Antenna Patterns

Examples of the resulting transmitter antenna gains expressed as a function of off-boresight angles θ^B are depicted in Fig. 11. To highlight the repeatability of the G_T solutions from this process, Fig. 11(a) depicts derived patterns from each of the eight receivers, derived independently, and reported separately where it can be observed that, for this block, IIR transmitter peak deviation is limited to 0.2 dB relative to the mean. Compared to reference patterns [14], both sets exhibit a similar behavior characterized by a gradual increase of gain peaking at $\approx 10^\circ$. However, the solutions suggest that peak SVN 41 gains are on the order of 17 dB, while the reference suggests a 16-dB peak gain. Importantly, for the purposes of calibrating CYGNSS's observables, the difference between the two sets of patterns is not a constant and instead includes a shape modification. It is this form of shape adjustment that is thought to be more representative of in-orbit behaviors, thereby contributing to more improved calibration quality through facilitating more accurate ratio estimates in (5).

Other examples include the block IIF case study involving SVN 70 in Fig. 11(b) where derived G_T patterns are reported across the three main roll states to highlight the independence of the solutions from the receivers' attitudes as a result, in part, of the improved zenith gain pattern estimates where peak deviation is similarly limited to less than 0.1–0.2 dB. Block IIF patterns are characterized by limited variability of gain levels, increasing by no more than 0.5 dB, up to an angle $\theta^B = 10^\circ$

Authorized licensed use limited to: University of Michigan Library. Downloaded on July 22,2026 at 17:41:03 UTC from IEEE Xplore. Restrictions apply.

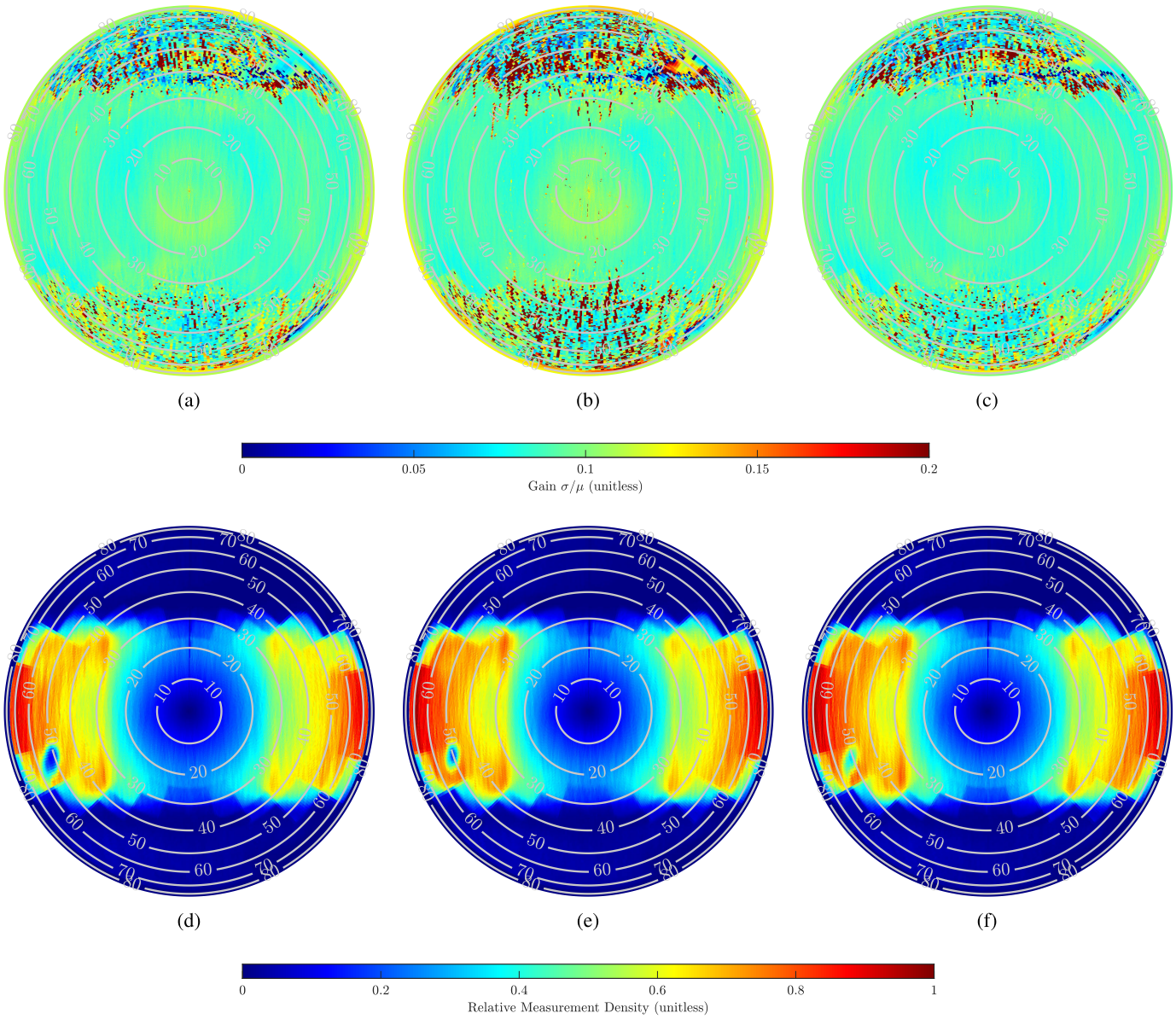


Fig. 10. Relevant gain solutions' uncertainty statistics. (a) Uncertainty, FM01. (b) Uncertainty, FM02. (c) Uncertainty, FM05. (d) Measurement density, FM01. (e) Measurement density, FM02. (f) Measurement density, FM02.

followed by a less gradual decline in gain levels. Depending on θ^B, the differences relative to the reference estimates vary between 1.5–3 dB, but CYGNSS's derived patterns suggest that G_T levels are consistently higher than published levels. For other block IIF patterns, the mean difference is on the order of 0.5–0.75 dB.

The case study summarized in Fig. 11(c) explores the more complex scenario of SVN 80, a block III GPS transmitter, where no reference is available. For ease of visual comparisons with other pertinent SVNs, its G_T is given as an "anomaly" where the zero mean function is reported after subtracting the mean 15.13-dB gain level. As part of a GPS modernization and transmitter replenishment effort, block III satellites were designed to serve as next-generation transmitters equipped with upgraded payloads that enable improved jamming resilience, the capacity to transmit the additional civilian signal L1C, and operation over a nominal life cycle of 15 years. The first block III satellite was launched in December 2018 and began operations soon after. While recent analyses [18], [19] have attempted to characterize the properties of block III satellites using ground-based monitors, for SVN 80, which began operations as recently as December 2024, no public reference characterizations are known to be available. As a result, given the need for the placement of constraints on the range of G_T solutions in the process contributing to the development of $G^{R,Z}$ solutions, no block III observations were initially incorporated. The case of SVN 80 is an illustrative example of the broader issue of requiring to consistently populate transmitter SVN gain tables to support ongoing calibration activities, including future SVNs, where no public references may be available.

Authorized licensed use limited to: University of Michigan Library. Downloaded on July 22,2026 at 17:41:03 UTC from IEEE Xplore. Restrictions apply.

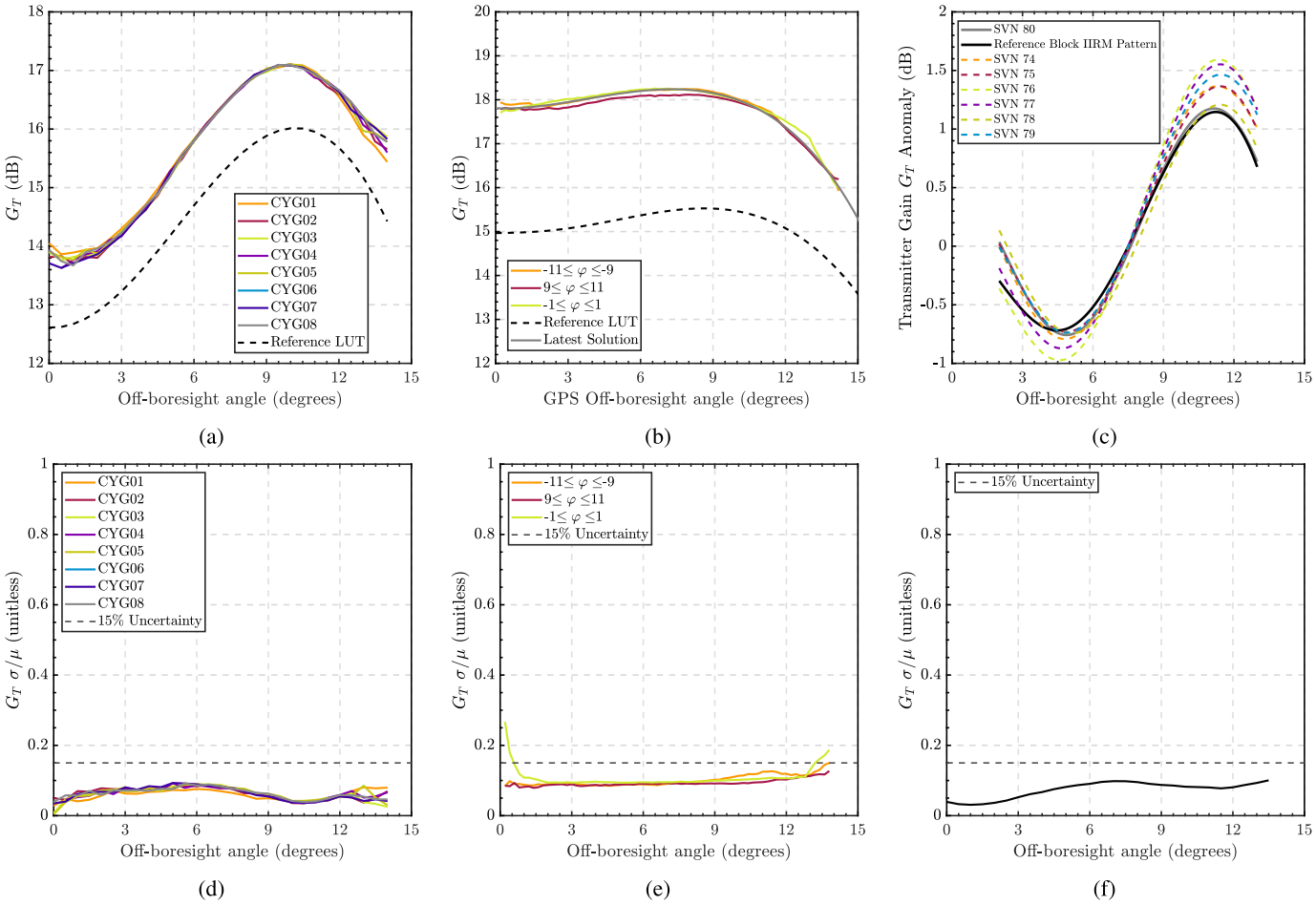


Fig. 11. Example GPS G_T patterns rederived using CYGNSS's zenith channels and related uncertainty statistics. (a) Pattern, SVN 41 as an example of a block IIR transmitter. (b) Pattern, SVN 70, as an example of a block IIF transmitter. (c) Pattern, SVN 80, as an example of a block III transmitter. For ease of visual comparison, it is reported as an "anomaly" after subtracting its constant 15.13-dB mean from all off-boresight angle gain levels. (d) Solution uncertainty, SVN 41. (e) Solution uncertainty, SVN 70. (f) Solution uncertainty, SVN 80.

It is instructive to note that in Section III, the limited range of ancillary inputs incorporated was added as a precaution given the underdetermined nature of the system of equations, which was initially available where both the receiver's gain patterns and the transmitter's gain patterns were unknown. However, once a satisfactory set of receiver zenith gain patterns is derived, the solution for all future G_T estimates is simply given by a rearrangement of the terms in (4).

In the case of SVN 80, a $P_T = 300$ W is selected following the assumed values reported in the relevant literature [20]. While this enables estimating absolute gain levels, related uncertainties have limited impact on CYGNSS's calibration as it is ratios of gain at different off-boresight angles that are utilized as part of the calibration process in (5). Overestimates of P_T shift the complete curve to a lower mean gain level, while underestimates of P_T shift up the overall gain curves to a higher mean gain level. In both cases, the impact is negated by a cancellation of the multiplicative term P_T.

The SVN 80, block III, antenna pattern exhibits a more complex variability of gain levels characterized by a systematic decrease up to $\theta^B = 6°$ followed by a 5-dB increase peaking at $\theta^B = 11.5°$. In addition, examples relating to preceding block III SVNs such as 74–79 are also depicted in Fig. 11(c) whose patterns are consistent with a variety of independent measurements previously reported [18], [19]. For additional, more qualitative validation, the block IIRM patterns are also included. In spite of the process of deriving the G_T patterns corresponding to SVNs 74–80 not being aided by any ancillary inputs, the overall gain curves exhibit a noteworthy likeness to published block IIRM patterns. It is helpful to note that while block IIF transmitters were manufactured by the Boeing Company, block IIRM and block III SVNs are manufactured by the Lockheed Martin Corporation such that the trends in Fig. 11(c) suggest that the same antenna modules were used across both fleets.

The final G_T is a per-FM mean across all receivers and all roll states. While the averaging reduces the noise associated with estimates of G_T deriving from a single polar pixel, it is of interest to explore the uncertainty associated with the complete set of solutions using the proposed methodology as a means of quantifying variability. Example transmitter gain uncertainties given by their σ/μ are also depicted in Fig. 11(d)–(f). It can be observed that, irrespective of the specific CYGNSS receiver, the uncertainty estimates are highly repeatable across all three example SVNs. While most peak at 10% relative to the mean for the older generation transmitters such as SVN 41, across

Authorized licensed use limited to: University of Michigan Library. Downloaded on July 22,2026 at 17:41:03 UTC from IEEE Xplore. Restrictions apply.

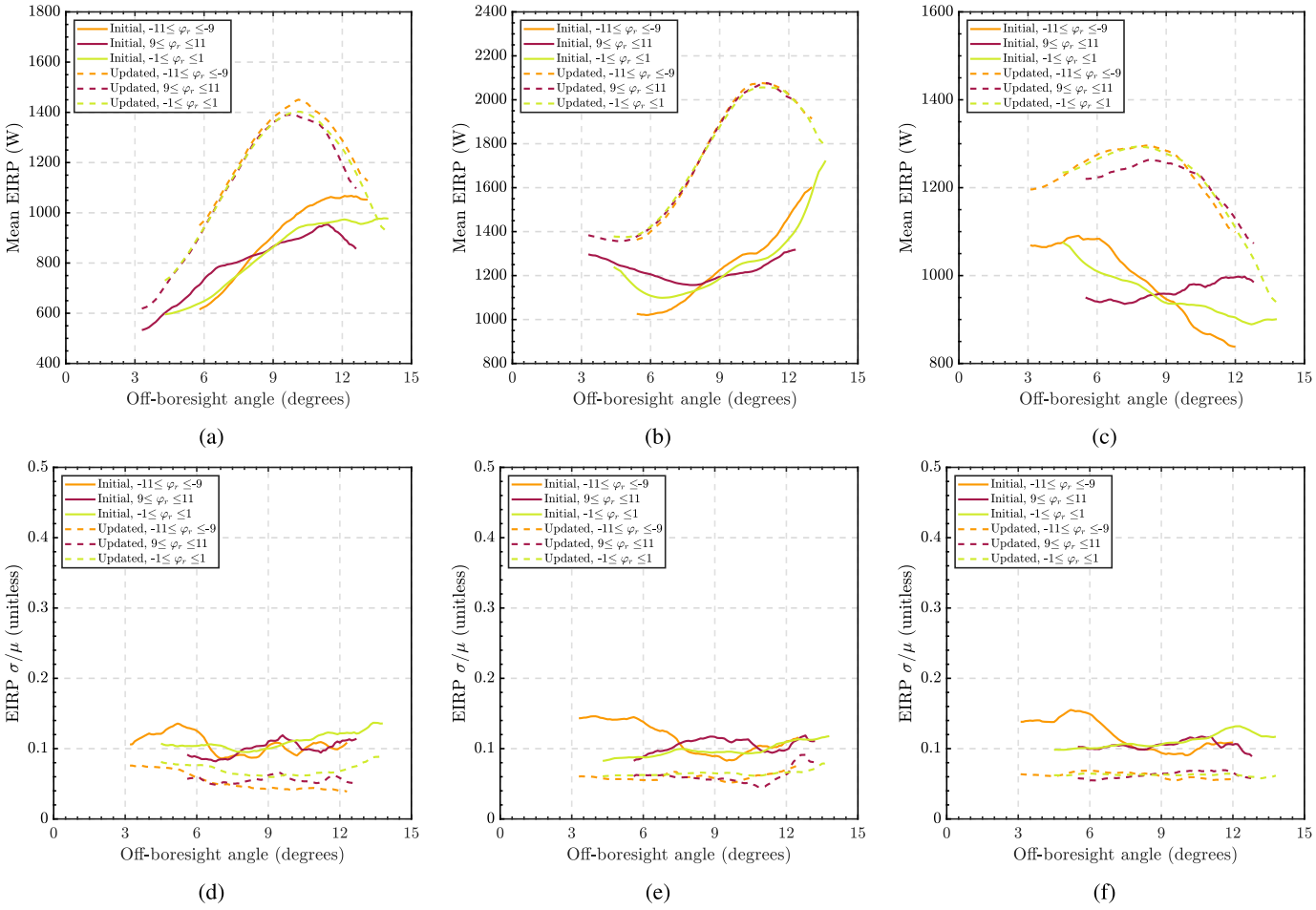


Fig. 12. Dynamically tracked EIRP statistics by CYGNSS zenith antennas using existing and updated patterns. (a) Mean EIRP, SVN 41 as an example of a block IIR transmitter. (b) Mean EIRP, SVN 58 as an example of a block IIRM transmitter. (c) Mean EIRP, SVN 71, as an example of a block IIF transmitter. (d) Uncertainty, SVN 41. (e) Uncertainty, SVN 58. (f) Uncertainty, SVN 71.

all transmitters, the mean uncertainty is estimated to be on the order of 4%, highlighting the repeatability of G_T estimates across all FMs, roll states, and polar subsets of the zenith antenna patterns used.

C. EIRP Trends

The impact of the updated patterns on EIRP trends is explored using the example block IIR, IIRM, and IIF measured EIRPs originating from SVNs 41, 58, and 71, respectively, in Fig. 12. It is instructive to recall, from (4), that over periods during which the transmitters are not operated in a "flex power" mode, it is most accessible to consider mean EIRP as merely a G_T function scaled by a constant P_T such that, for well-calibrated zenith measurements, the shapes of the EIRP curves should be expected to mirror their corresponding G_T estimates, examples of which were depicted in Fig. 11. The trends depicted in Fig. 12 highlight the effects of incorporating the updated patterns as, irrespective of SVN, the measured EIRP trends for every block type closely mimic expected behaviors. Conversely, the impacts of preceding mischaracterizations can also be observed where, depending on roll state, significant shape distortions can occur. Examples of this include the local peak at $\varphi_r = +10^\circ$ and $\theta^B = 11$ that is not suggested by the derived G_T patterns or published reference patterns. Similar, more egregious, shape distortions across all three roll angles are noted for SVN 58 and all other block IIRM SVNs whose reflections not only do not resemble the corresponding block IIRM curves but also exhibit distinct shapes across the three roll states. While uncertainties in published G_T estimates contribute to these effects, the majority of the observed shape distortions are thought to be attributable to uncertainties in zenith antenna patterns informed by initial characterizations. Recall both the mapping of measurements to distinct spaces (i.e., "ring structures") in Fig. 6 and the nonuniform gain differences of the updated compared to the existing patterns exhibited in Fig. 9. A relevant figure of merit is, therefore, the relative shape distortion ζ^S

$$\zeta^S = \frac{100}{N_{G_T}} \sum_{i=1}^{N_{G_T}} \frac{\left| \overline{E}^{Z,S}(i) - \overline{G}_T(i) \right|}{\overline{G}_T(i)} \tag{14}$$

comparing the normalized, to a scale of zero to one, EIRP functions to their corresponding G_T functions. The resulting mean estimates for block types IIR, IIRM, IIF, and III using the updated patterns are 6.68%, 4.09%, 2.89%, and 6.48%. The mean shape distortion using the initial zenith patterns is 69.64%.

Authorized licensed use limited to: University of Michigan Library. Downloaded on July 22,2026 at 17:41:03 UTC from IEEE Xplore. Restrictions apply.

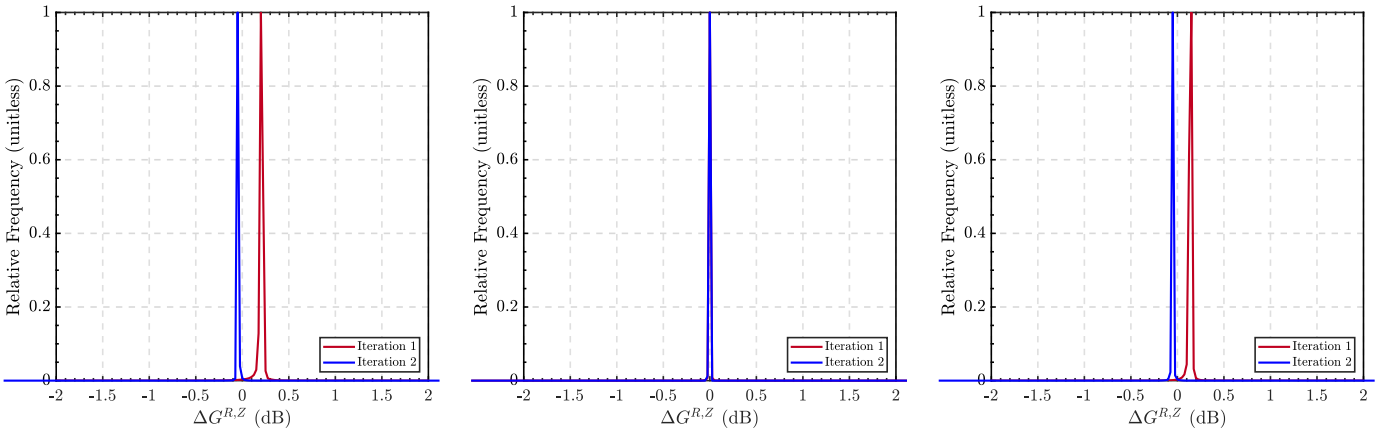


Fig. 13. Zenith antenna pattern difference distributions following an iterative procedure derivation procedure that interrogates the impact of feedback between the correction intended to account for digital sampling artifacts and zenith gain patterns. (a) FM01. (b) FM04. (c) FM08.

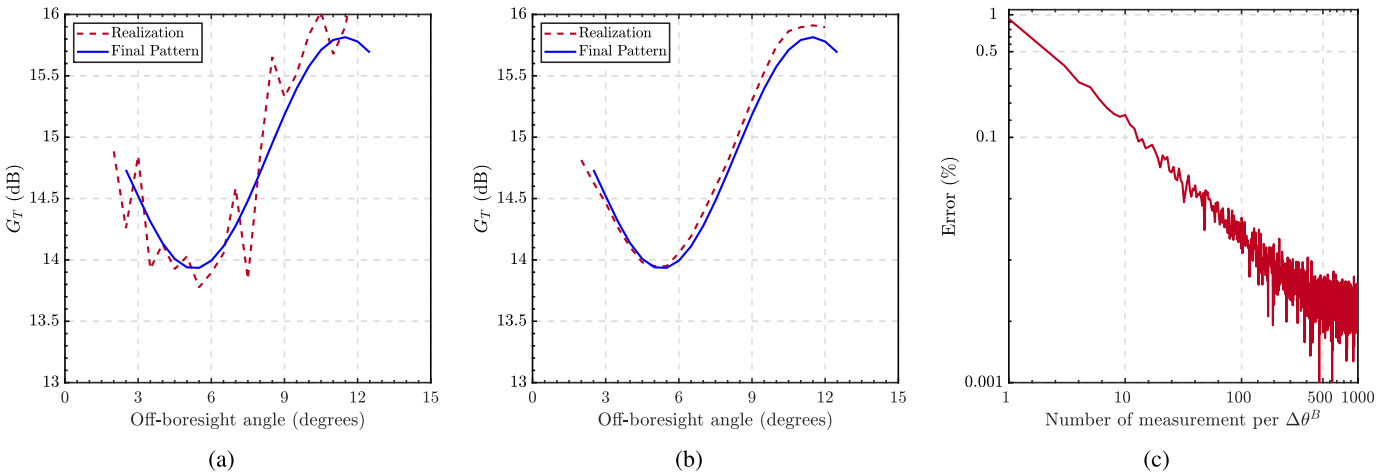


Fig. 14. Analysis pertaining to the number of measurements required to derive SVN's G_T patterns explored using the example of SVN 81. (a) One measurement per $\Delta\theta^B$, all randomly selected. (b) 1000 measurements per $\Delta\theta^B$, all randomly selected. (c) Error as a function of number of measurements per $\Delta\theta^B$.

As millions of measurements contribute to the observed means in Fig. 12 at a given θ^B angle, it is also of interest to explore the corresponding uncertainty statistics also depicted in Fig. 12. Using both sets of input patterns, it is observed that uncertainties are limited to peak levels of 15% with similar shape distortions using the original inputs occasionally impacting uncertainty levels at specific θ^B angles. Nonetheless, a consistent improvement with the revised inputs is achieved where, in the case of the example SVNs depicted in Fig. 12, uncertainty values as low as 5% are attained, representing 50%–60% reductions compared to their original levels. The resulting overall mean uncertainty estimates for all block types are, on average, reduced by 33.09%.

V. Practical Considerations

A. Need for Iterative Procedure

The EIRP calibration procedure highlights the need to apply multiple correction terms. Two are of particular interest: Λ and $G^{R,Z}$. Determination of the appropriate ν_Z for each of the eight zenith channels is based on a process that minimizes the slopes of measured, dynamic P_T estimates as a function of bin ratios. For a comprehensive overview, see [16]. These measured P_T values are obtained by rearranging the terms in (4) such that the absolute magnitude of CYGNSS's reported SVN-specific P_T is impacted by both ν_Z and $G^{R,Z}$. While this may suggest that an iterative procedure may be needed for the determination of both, tests suggest that iterations beyond the initial assessments have minimal effect on either solution. To illustrate this, the results of this iterative procedure in the context of derived zenith antenna gains are described in Fig. 13 using the examples of FM01, FM04, and FM07. Appropriate initial $\nu_{Z,i}$ terms are determined using a version of the calibration procedure that incorporates initial characterizations of the gain patterns. Once $\nu_{Z,i}$ is determined, the procedures described in Section III are implemented to derive the initial version of the zenith antenna patterns $G^{R,Z,i}$. The process of determining parameters pertinent to the Λ function is then repeated using a calibration procedure that incorporates $G^{R,Z,i}$, giving rise to $\nu_{Z,1}$, which is then used to determine an updated $G^{R,Z,1}$. Iteration 1 summarizes the deviations between $G^{R,Z,1}$ and $G^{R,Z,i}$ where the differences are found to be limited to a peak of

Authorized licensed use limited to: University of Michigan Library. Downloaded on July 22,2026 at 17:41:03 UTC from IEEE Xplore. Restrictions apply.

0.25 dB for FM01 across the zenith pattern's complete polar space, 0.04 dB for FM04, and 0.2 dB for FM08. The procedure is repeated again with the resulting differences denoted by Iteration 2 in Fig. 13. While the further reduction of gain differences suggests that iterations refine the patterns, both sets of differences highlight that convergence is achieved rapidly such that only applications sensitive to 0.02–0.25-dB level differences would need to pursue multiple iterations in the process of determining zenith antenna gain patterns. In the case of CYGNSS, the mean Iteration 1 differences were 0.22, 0.09, 0.02, 0.02, 0.06, 0.18, 0.12, and 0.15 dB across FM01–FM08, respectively, such that an iterative procedure is not deemed necessary. In addition, ν_Z solutions across all iterations are consistent within a 5% margin.

B. Measurement Density: Transmitter Gain Patterns

As new SVNs are brought online, a need arises to characterize their respective $G_T(\theta^B)$ patterns to be used in the Level-1 calibration algorithm. To that end, it is of interest to determine the number of measurements required to adequately characterize the pattern. This is explored through a Monte Carlo analysis using the case study of SVN 81, brought into operation in June 2025. Using more than 200 000 SVN 81 measurements tracked since, the pattern's final form is derived and reported in Fig. 14. Subsequently, the impact of measurement density on the capacity to reconstruct the pattern is explored by varying the number of measurements in each $\Delta\theta^B = 0.5^\circ$ bin. In the case of Fig. 14(a), one measurement per $\Delta\theta^B$ is randomly selected, while, in Fig. 14(b), 1000 measurements per $\Delta\theta^B$ are randomly selected and subsequently averaged. While, in both cases, the envelope of the pattern is adequately captured, the improvements that the larger number of measurements yields are readily identifiable. The same analysis is repeated across 200 realizations, and the mean relative error is reported in Fig. 14(c) where it is observed that ≈ 100 measurements per $\Delta\theta^B$ are sufficient for recreating, effectively, the same reference pattern. For a receiver operating with a duty cycle comparable to CYGNSS, a single day of data would be sufficient to accumulate the necessary number of measurements.

VI. Conclusion

This work sought to highlight how CYGNSS's in-orbit roll maneuvers may be used for calibration diagnostics and improvement. This is achieved in large part through the diversities that arise in observation geometries, which occur at distinct GPS off-boresight angles, corresponding to each roll state, even at fixed zenith pattern polar locations. As a result, the consistency of calibration may be interrogated using EIRP anomalies across the different roll angles relative to a nonrolled state such that a perfectly calibrated system would exhibit limited variability as a function of θ^B. Subsequently, these properties were leveraged as a means of deriving improved zenith antenna pattern estimates, as well as GPS G_T, which were shown to improve the overall consistency of reported, dynamically tracked, EIRPs.

The utility of the roll maneuvers for achieving further improvements to the constellation's nadir antenna patterns and assessing the overall impact they have on the quality of observables is explored in Part II of this work.

References

[1] S. Gleason and V. Zavorotny, "Bistatic radar cross section measurements of ocean scattered GPS signals from low Earth orbit," in *Proc. IEEE Int. Symp. Geosci. Remote Sens.*, Jul. 2006, pp. 1308–1311, doi: 10.1109/IGARSS.2006.338.

[2] J. Park, J. T. Johnson, A. O'Brien, and S. T. Lowe, "Studies of TDS-1 GNSS-R ocean altimetry using a 'full DDM' retrieval approach," in *Proc. IEEE Int. Geosci. Remote Sens. Symp. (IGARSS)*, Jul. 2016, pp. 5625–5626, doi: 10.1109/IGARSS.2016.7730469.

[3] C. Ruf et al., *CYGNSS Handbook*, 2nd ed., Ann Arbor, MI, USA: Michigan Publishing, 2022.

[4] M. J. Unwin et al., "An introduction to the HydroGNSS GNSS reflectometry remote sensing mission," *IEEE J. Sel. Topics Appl. Earth Observ. Remote Sens.*, vol. 14, pp. 6987–6999, 2021, doi: 10.1109/JSTARS.2021.3089550.

[5] F. Huang et al., "Spaceborne GNSS reflectometry with Galileo signals on FY-3E/GNOS-II: Measurements, calibration, and wind speed retrieval," *IEEE Geosci. Remote Sens. Lett.*, vol. 20, pp. 1–5, 2023, doi: 10.1109/LGRS.2023.3241358.

[6] F. Huang et al., "Tianmu-1 constellation GNSS-R in-orbit performance: Spatiotemporal characteristics, product applications, and polarimetric features," *IEEE Trans. Geosci. Remote Sens.*, vol. 63, 2025, Art. no. 5802020, doi: 10.1109/TGRS.2025.3581343.

[7] D. Masters et al., "Status and plans for spire's growing commercial constellation of GNSS science cubesats," in *Proc. Joint 6th ROM SAF User Workshop 7th IROWG*, Sep. 2019, pp. 1–23.

[8] M. Roberts, I. Colwell, C. Chew, D. Masters, and K. Nordstrom, "The Muon space GNSS-R surface soil moisture product," 2024, *arXiv:2412.00072*.

[9] S. Gleason and C. Ruf, "Overview of the delay Doppler mapping instrument (DDMI) for the cyclone global navigation satellite systems mission (CYGNSS)," in *IEEE MTT-S Int. Microw. Symp. Dig.*, May 2015, pp. 1–4, doi: 10.1109/MWSYM.2015.7166775.

[10] S. Gleason, M. Al-Khaldi, and D. McKague, "Cyclone global navigation satellite system (CYGNSS): Algorithm theoretical basis document level 1A DDM calibration," NASA/Univ. Michigan, Ann Arbor, MI, USA, Tech. Rep. 148-0136, 2023.

[11] S. Gleason, M. Al-Khaldi, and D. McKague, "Cyclone global navigation satellite system (CYGNSS): Algorithm theoretical basis document level 1B DDM calibration," NASA/Univ. Michigan, Ann Arbor, MI, USA, Tech. Rep. 148-0137, 2023.

[12] T. Wang, C. S. Ruf, B. Block, D. S. McKague, and S. Gleason, "Design and performance of a GPS constellation power monitor system for improved CYGNSS L1B calibration," *IEEE J. Sel. Topics Appl. Earth Observ. Remote Sens.*, vol. 12, no. 1, pp. 26–36, Jan. 2019, doi: 10.1109/JSTARS.2018.2867773.

[13] T. Wang et al., "Dynamic calibration of GPS effective isotropic radiated power for GNSS-reflectometry Earth remote sensing," *IEEE Trans. Geosci. Remote Sens.*, vol. 60, 2022, Art. no. 5800512, doi: 10.1109/TGRS.2021.3070238.

[14] W. Marquis, "The GPS block IIR/IIR-M antenna panel pattern," Lockheed Martin Corp., Bethesda, MD, USA, Tech. Rep. LMCO-2014, 2014.

[15] M. M. Al-Khaldi et al., "Detection and analysis of GPS L1-band radio frequency interference using spaceborne global navigation satellite system reflectometry receivers," *IEEE Trans. Geosci. Remote Sens.*, vol. 63, 2025, Art. no. 5802214, doi: 10.1109/TGRS.2025.3584367.

[16] S. Gleason, M. M. Al-Khaldi, C. S. Ruf, D. S. McKague, T. Wang, and A. Russel, "Characterizing and mitigating digital sampling effects on the CYGNSS level 1 calibration," *IEEE Trans. Geosci. Remote Sens.*, vol. 60, 2022, Art. no. 5802812, doi: 10.1109/TGRS.2021.3120026.

[17] T. Wang et al., "Measurement of GPS antenna gain patterns for CYGNSS using a spaceborne antenna range," *IEEE Trans. Aerosp. Electron. Syst.*, vol. 60, no. 5, pp. 6883–6893, Oct. 2024, doi: 10.1109/TAES.2024.3414961.

[18] P. Steigenberger, S. Thoelert, R. Dach, and O. Montenbruck, "Validation of GPS III transmit antenna calibrations," *Adv. Space Res.*, vol. 73, no. 5, pp. 2488–2498, Mar. 2024, doi: 10.1016/j.asr.2023.11.048.

[19] S. Thoelert, P. Steigenberger, O. Montenbruck, and M. Meurer, "Signal analysis of the first GPS III satellite," *GPS Solutions*, vol. 23, no. 4, pp. 1–21, Jul. 2019, doi: 10.1007/s10291-019-0882-7.

[20] P. Steigenberger, S. Thoelert, and O. Montenbruck, "GPS and GLONASS satellite transmit power," German Space Operations Center, Weßling, Germany, Tech. Rep. DLR/GSOC TN 19-01, 2019.

Authorized licensed use limited to: University of Michigan Library. Downloaded on July 22,2026 at 17:41:03 UTC from IEEE Xplore. Restrictions apply.



Mohammad M. Al-Khaldi (Member, IEEE) received the bachelor's degree in electrical engineering from American University of Sharjah, Sharjah, United Arab Emirates, in 2015, the M.S. degree in electrical engineering from Texas A&M University, College Station, TX, USA, in 2017, the second M.S. degree in electrical and computer engineering from The Ohio State University, Columbus, OH, USA, in 2019, and the Ph.D. degree from the Department of Electrical and Computer Engineering and ElectroScience Laboratory, The Ohio State University in 2020.

He was previously a Project Scientist I, a Post-Doctoral Fellow II, and a Post-Doctoral Fellow I of the Cosmic Program with the University Corporation for Atmospheric Research (UCAR), Boulder, CO, USA. He is currently a Research Scientist at the ElectroScience Laboratory and Department of Electrical and Computer Engineering, The Ohio State University. His research interests include applied electromagnetics, rough surface scattering, and spaceborne remote sensing.

Dr. Al-Khaldi has been a member of NASA CYGNSS Mission Science Team, NASA CYGNSS Mission Calibration and Validation Team, NASA GNSS Science Team, IEEE GRSS Technical Committee on Modeling in Remote Sensing, IEEE GRSS Technical Committees on Frequency Allocations in Remote Sensing, has been an Associate Member of Commissions B and F of the International Union of Radio Science (URSI), has been the NASA CSDA GNSS-R Subject Matter Expert (SME), and served as an Associate Editor for *Radio Science* and a Topical Associate Editor for IEEE TRANSACTIONS ON GEOSCIENCE AND REMOTE SENSING.



Scott Gleason (Senior Member, IEEE) received the B.S. degree in electrical and computer engineering from the State University of New York at Buffalo, Buffalo, NY, USA, in 1991, the M.S. degree in engineering from Stanford University, Stanford, CA, USA, in 1999, and the Ph.D. degree in applied physics from the University of Surrey, Surrey, U.K., in 2007.

He is currently the President of Daaxa LLC Consulting Company, Boulder, CO, USA, specializing in GNSS instruments, calibration, and remote sensing applications. He is the Co-Investigator on the Science Team and Instrument Scientist for the NASA CYGNSS Mission. He has worked in the areas of astronautics, remote sensing, and global navigation satellite systems for more than 20 years, including at NASAs Goddard Space Flight Center, Greenbelt, MD, USA, GPS Laboratory, Stanford University, CA, USA, Surrey Satellite Technology Ltd., Guildford, U.K., Concordia University, Montreal, QC, Canada, Southwest Research Institute, San Antonio, TX, USA, the University Corporation for Atmospheric Research (UCRS), Boulder, CO, USA, and the National Oceanography Centre, Southampton, U.K.



Christopher S. Ruf (Life Fellow, IEEE) received the B.A. degree in physics from Reed College, Portland, OR, USA, in 1982, and the Ph.D. degree in electrical and computer engineering from the University of Massachusetts at Amherst, Amherst, MA, USA, in 1987.

He is currently the Frederick Bartman Collegiate Professor of climate and space science and the Director of the Space Institute, University of Michigan, Ann Arbor, MI, USA, and the Principal Investigator of the NASA CYGNSS Mission. He has worked previously for Intel Corporation, Aloha, OR, USA, Hughes Space and Communication, El Segundo, CA, USA, the NASA Jet Propulsion Laboratory, Pasadena, CA, USA, and Penn State University, University Park, PA, USA. His research interests include remote sensing methods, applications, and technology.

Prof. Ruf is a member of the National Academy of Engineering, a fellow of American Meteorological Society, the Vice Chair for Commission F of U.S. National Committee of the International Radio Science Union, and a member of American Geophysical Union. He is the Former Editor-in-Chief of IEEE Transactions on Geoscience and Remote Sensing and has served on the Editorial Board for *Radio Science*, the JOURNAL OF ATMOSPHERIC AND OCEANIC TECHNOLOGY, and *Scientific Reports*.



Joel T. Johnson (Fellow, IEEE) received the bachelor's degree in electrical engineering from Georgia Institute of Technology, Atlanta, GA, USA, in 1991, and the S.M. and Ph.D. degrees from Massachusetts Institute of Technology, Cambridge, MA, USA, in 1993 and 1996, respectively.

He is currently a Professor with the ElectroScience Laboratory, Department of Electrical and Computer Engineering, The Ohio State University, Columbus, OH, USA. His research interests include the areas of microwave remote sensing, propagation, and electromagnetic wave theory.

Dr. Johnson is a member of Commissions B and F of the International Union of Radio Science (URSI), Tau Beta Pi, Eta Kappa Nu, and Phi Kappa Phi. He received the 1993 Best Paper Award from IEEE Geoscience and Remote Sensing Society, was named an Office of Naval Research Young Investigator, the National Science Foundation Career Awardee, and the PECASE Award Recipient in 1997, and was recognized by U.S. National Committee of URSI as a Booker Fellow in 2002. He has served as the Technical Program Co-Chair for the 2017 International Geoscience and Remote Sensing Symposium. He has been serving as an Associate Editor for IEEE TRANSACTIONS ON GEOSCIENCE AND REMOTE SENSING since 2000. He is also the Past Chair of GRSS Technical Committee on Frequency Allocations in Remote Sensing.



Darren S. McKague (Member, IEEE) received the Ph.D. degree in astrophysical, planetary, and atmospheric sciences from the University of Colorado, Boulder, Boulder, CA, USA, in 2001.

He is an Associate Research Scientist with the Department of Climate and Space Sciences and Engineering, University of Michigan, Ann Arbor, MI, USA. Prior to working for Michigan, he worked as a Systems Engineer for Ball Aerospace and Raytheon, and as a Research Scientist at Colorado State University, Fort Collins, CO, USA. His work has focused on remote sensing with an emphasis on the development of spaceborne microwave remote sensing hardware, microwave remote sensor calibration techniques, and mathematical inversion techniques for geophysical retrievals. His experience with remote sensing hardware includes systems engineering for several advanced passive and active instrument concepts and the design of the calibration subsystem on the Global Precipitation Mission (GPM) Microwave Imager (GMI), as well as the development of calibration and intercalibration techniques for the GPM constellation. His algorithm experience includes the development of a near-real time algorithm for the joint retrieval of water vapor profiles, temperature profiles, cloud liquid water path, and surface emissivity for the advanced microwave sounding unit (AMSU) at Colorado State University, and the development of the precipitation rate, precipitation type, sea ice, and sea surface wind direction algorithms for the risk reduction phase of the conical scanning microwave imager/sounder (CMIS).



Anthony Russel received the B.S. degree in computer science engineering from Michigan State University, East Lansing, MI, USA, in 2014.

He was a member of the Engineering Staff with the Space Physics Research Laboratory, College of Engineering, University of Michigan, Ann Arbor, MI, USA. He is now a Software Engineer at Muon Space, Mountain View, CA, USA. His primary engineering activities involve algorithm development and large-scale data processing.

Authorized licensed use limited to: University of Michigan Library. Downloaded on July 22,2026 at 17:41:03 UTC from IEEE Xplore. Restrictions apply.



William L. Wells received the bachelor's degree in aerospace engineering from The University of Texas at Austin, Austin, TX, USA, in 2006.

He is a Staff Systems Engineer with the Department of Space Instrumentation, Southwest Research Institute, San Antonio, TX, USA. He received over 17 years of experience spanning all phases of space mission development and execution. His career focus is systems engineering for constellation missions. He is concurrently the Operations Phase Systems Engineering Lead for the Cyclone Global Navigation Satellite System (CYGNSS) Mission and the Project Systems Engineer for the Polarimeter to Unify the Corona and Heliosphere (PUNCH) Mission.



Tianlin Wang (Senior Member, IEEE) received the B.E. degree in electrical engineering from East China University of Science and Technology, Shanghai, China, in 2009, the M.S. degree in radio physics from Fudan University, Shanghai, in 2012, and the Ph.D. degree in electrical engineering from the University of Michigan, Ann Arbor, MI, USA, in 2021.

He is currently a Research Technologist with the Earth Science Section, Jet Propulsion Laboratory, California Institute of Technology, Pasadena, CA, USA. Prior to this, he was a President's Post-Doctoral Scholar with the Department of Electrical and Computer Engineering and the ElectroScience Laboratory, The Ohio State University, Columbus, OH, USA, from 2021 to 2023. His research interests include microwave remote sensing, microwave measurements, radio frequency (RF) circuits, and wave propagation and scattering.

Dr. Wang is a member of Tau Beta Pi, Eta Kappa Nu, and the American Geophysical Union (AGU). He received the 2018 IEEE Mikio Takagi StudentPrize, an Outstanding Student Presentation Award from the 2018 AGU Fall Meeting, the 2021 Ernest K. Smith USNC-URSI Student Prize (second place), and the Young Scientist Awards from the 44th Photonics and Electromagnetics Research Symposium and the XXXVth URSI General Assembly and Scientific Symposium in 2023. He currently serves as the Chair for the Modeling in Remote Sensing (MIRS) Technical Committee and the Chapters Committee of IEEE Geoscience and Remote Sensing Society (GRSS).



Dorina Twigg received the B.S.E. degree in computer engineering from the University of Michigan, Ann Arbor, MI, USA, in 1991, and the M.S. degree in computer science from Wayne State, Detroit, MI, USA, in 2012.

She is a Member of the Engineering Staff with the Space Physics Research Laboratory, College of Engineering, University of Michigan, Ann Arbor, MI, USA, and has a lead role in satellite commanding and scientific data processing with the Science Operations Center for the CYGNSS NASA Earth Venture mission.

Patrick McEnaney, photograph and biography not available at the time of publication.

Joshua Synowiec, photograph and biography not available at the time of publication.

Authorized licensed use limited to: University of Michigan Library. Downloaded on July 22,2026 at 17:41:03 UTC from IEEE Xplore. Restrictions apply.